RSC Advances

This article can be cited before page numbers have been issued, to do this please use: S. Saha, M. Jana, P. Khanra, P. Samanta, H. Y. Koo, N. C. Murmu and T. Kuila, *RSC Adv.*, 2015, DOI: 10.1039/C5RA20928E.

ROYAL SOCIETY OF CHEMISTRY

www.rsc.org/advances

View Article Online
DOI: 10.1039/C5RA20928E

RSC Advances

ARTICLE

Band gap modified boron doped NiO/Fe_3O_4 nanostructure as the positive electrode for high energy asymmetric supercapacitor

Received 00th January 20xx,
Accepted 00th January 20xx

DOI: 10.1039/x0xx00000x

www.rsc.org/

Sanjit Saha,[a,b] Milan Jana,[a,b] Partha Khanra,[c] Pranab Samanta,[a,b] Hyeyoung Koo,[d] Naresh Chandra Murmu,[b] and Tapas Kuila [a*]

The boron doped NiO/Fe_3O_4 nanostructure was successfully synthesized by facile one-step hydrothermal method. The boron doping was confirmed from the decreased band gap energy and increased electrical conductivity of the NiO/Fe_3O_4 composite. The nyquist plot of the multi metal oxide was fitted with ZView software for the detailed understanding of the effect of concentration of different metal oxide, boron doping and extensive charge-discharge cycles on the electrochemical properties of the electrode materials. Very high specific capacitance of ~1467 F g^{-1} was achieved as the synergistic effect of low activation energy and short ion diffusion path of the electrode materials. Asymmetric supercapacitor (ASS) was fabricated by NiO/Fe_3O_4 composite and thermally reduced graphene oxide as positive and negative electrode, respectively. The ASS showed large specific capacitance of ~377 F g^{-1} at a current density of 3 A g^{-1}. Furthermore, the ASS showed a large energy density of ~102.6 W h kg^{-1}, huge power density of ~6300 W kg^{-1} and remained ~82% stable even after 10,000 charge discharge cycles. Therefore, a facile hydrothermal method was demonstrated to enhance the electrochemical properties of the multi metal oxide by boron doping for the development of next generation energy storage device.

Introduction

The development of next-generation economical, flexible, light-weight and renewable energy storage system is strongly required to meet the future demand of the portable and flexible electronics in modern society.[1-3] In this realm, electrochemical supercapacitors (ESs) have received considerable attention as high-performance energy storage devices since they can provide better capacitance, elevated power density, faster charge-discharge cycles, and long cycle life as compared to traditional lead-acid batteries or lithium-ion batteries.[1,4,5] However, the low energy density is the major limitation of the commercially available ESs.[6-8] The use of asymmetric configuration by utilizing both faradic and non-faradic charge storage mechanism can be a green and non hazardous solution to improve the operating voltage as well as the energy density of the ESs.[4,9-12] Carbonaceous materials like carbon nano tube, reduced graphene oxide (RGO) and CVD grown graphene are the proper choice as the negative electrode materials in supercapacitor device due to their electrochemical double layer capacitance (EDLC) charge storage mechanism.[9,12,13] On the other hand, conductive polymers and different transition metal oxides/hydroxides with rich pseudo-capacitance are widely used as positive electrode materials to enlarge the operating voltage as well as the energy storage capacity.[1,11,14]

The fast redox reactions due to the surface faradic process at an appropriate potential is the origin of the pseudocapacitance.[11] The smaller size and higher surface area of the electrode materials effectively reduce the diffusion path of electrolyte ions, facilitating ionic motion and improves the pseudo activity.[11] The porous materials can simultaneously adsorb and retain electrolyte ions resulting good faradic reaction even in the high current density.[15-17] However, the single-component nano-materials as electrodes show limitations due to the low electrical conductivity, rate capability and life stability.[11,14,15] An efficient approach to increase the rate capability of metal oxide/hydroxide positive electrode materials is to form hetero structure by the incorporation of one or two metal ions into their lattices.[11,15,16] The presence of hetero structure creates abundant structural defects and multiple accessible electro-active sites enhancing the redox reaction.[11,16] The nano-structured binary Ni-Fe oxide is one of the most promising hetero structure for supercapacitor applications due to their large theoretical capacitance value, deep average discharging profile and rich redox reactions.[11,17,18] The inter conversion between Fe(II) and Fe(III) provides redox capacitance for Fe_3O_4 in an aqueous electrolyte.[18]

[a] Surface Engineering & Tribology Division, CSIR-Central Mechanical Engineering Research Institute, Durgapur -713209, India
[b] Academy of Scientific and Innovative Research (AcSIR), CSIR-CMERI Campus, Durgapur-713209
[c] Soft Innovative Materials Research Centre, Korea Institute of Science and Technology (KIST), Jeonbuk 565905, South Korea
[d] Soft Innovative Materials Research Centre, Institute of Advanced Composite Materials, Korea Institute of Science and Technology (KIST), Jeonbuk 565905, South Korea
† Correspondence to Tapas Kuila. Tel.: +91-9647205077; Fax: 91-343-2548204
E-mail address: tkuila@gmail.com (Tapas Kuila)

Electronic Supplementary Information (ESI) available: XRD, FE-SEM, TEM, UV-vis spectroscopy, CV of NiO/Fe_3O_4 composite and the relation between diffusion time constant and activation energy. See DOI: 10.1039/x0xx00000x

View Article Online
DOI: 10.1039/C5RA20928E

NiO contributes to the pseudocapacitance based on the surface reversible redox mechanism[17]

$$NiO + OH^- \leftrightarrow NiOOH + e^-$$

NiO and Fe_3O_4 are the semiconducting materials with band gap energy of 3.6 - 4 eV and 1.92 - 2.87 eV, respectively.[19,20] The hetero structure of two different metal oxides is advantageous due to the size confinement of the highly enhanced electron-electron interactions.[21] The creation of defects or dislocations are highly expected due to the different lattice structure of the participating semiconductors which can create localized states by trapping the charge carriers and control the overall electrical characteristics of the system.[22] Furthermore, quantum interference effect can be reduced between the thin layer of the semiconducting hetero structure allowing enhanced ion exchange at the grain boundary.[22] The energy separation of two different band structures can create barrier and as a result the charge carriers can be confined allowing quasi-equilibrium potential state within the electrode.[12,22]

However, the large band gap or high electrical resistivity of NiO limits its applications. Therefore, superior electrochemical activity needs control on the electrical properties through proper doping of the materials.[12,23-26] In addition, control doping significantly increases the carrier concentration by creating free charge carriers.[25] Saha et al. have shown that the band gap modification of the insulating boron nitride is highly effective for electrochemical or supercapacitor applications.[12] Alver et al. have explained the effect of boron doping on the band structure and electrical conductivity of the NiO.[25] Chi et al. have shown that the supercapacitor performance of MnO_2 increases after boron doping.[26]

On the basis of the above considerations, one-step hydrothermal synthesis of boron doped NiO/Fe_3O_4 nano composite has been demonstrated. Nickel sulphate, Iron sulphate and boric acid were used as the source of nickel, iron and boron, respectively. The electrical conductivity of the NiO/Fe_3O_4 nanocomposite increases significantly due to the boron doping. The variation in the morphology of the composite can be observed with different ratio of nickel sulphate and iron sulphate precursor. Furthermore, the supercapacitive performance varied with the morphology of the nano structure and better results was obtained after boron doping. The asymmetric supercapacitor (ASS) cell was designed by using NiO/Fe_3O_4 composite as positive and thermally reduced graphene oxide (TRGO) as the negative electrode materials

Experimental

2.1 Reagents

Natural graphite flakes were purchased from Sigma-Aldrich. Hydrochloric acid, sulphuric acid, potassium permanganate, hydrogen peroxide, nickel sulphate, iron sulphate, boric acid, ammonia solution, N, N-dimethyl formamide (DMF) and potassium hydroxide were purchased from Merck, Mumbai, India. Conducting carbon black (EC-600JD, purity: >95%) and polyvinylidene fluoride (PVDF) were purchased from Akzo Nobel Amides Co., Ltd, South Korea. Nickel foam was purchased from Shanghai Winfay New Material Co., Ltd., China.

2.2 Preparation of boron doped NiO/Fe_3O_4 composites and TRGO

$NiSO_4$ (~2 g) and $FeSO_4$ (~2 g) were dissolved in ~60 ml of distilled water. The solution was taken into a 100 ml teflon lined autoclave. About 20 ml of ammonia solution was added and the autoclave was kept at 160 °C for 5 h. The product was collected by vacuum filtration (with distilled water and ethanol) and dried inside a vacuum oven at 50 °C. The sample was designated as FN. Another two samples, F1N2 and F2N1 were prepared by varying the concentration of $NiSO_4$ and $FeSO_4$. About 2 g of $NiSO_4$ and 1 g of $FeSO_4$ were taken for the preparation of F1N2. Similarly, about 1 g $NiSO_4$ and 2 g $FeSO_4$ were taken for the preparation of F2N1. F1N2B was prepared by adding 0.5 g boric acid to the autoclave keeping other parameters constant (same that of F1N2). Another three samples F1N2B1, F1N2B2 and F1N2B3 were prepared by increasing the concentration of boric acid. About 1, 1.5 and 2 g of boric acid was taken for F1N2B1, F1N2B2 and F1N2B3, respectively keeping other parameters constant. GO was prepared from natural graphite flake by modified Hummer's method.[12] Thermally reduced GO (TRGO) was prepared through the thermal reduction of GO (~100 mg) at 500 °C for ~15 min (under Ar gas atmosphere).

2.3 Structural and morphological characterization

X-ray diffraction (XRD) studies of the composite were carried out at room temperature on a D/Max 2500 V/PC (Rigaku Corporation, Tokyo, Japan) at a scan rate of 1° min^{-1} (Cu Kα radiation, λ = 0.15418 nm). The morphology of the NiO/Fe_3O_4 was measured by field emission scanning electron microscopy (FE-SEM) using Σigma HD, Carl Zeiss, Germany and transmission electron microscopy (TEM) was carried out using a JEOLTEM 2100 FS instrument (Japan) at 200 kV. X-ray photoelectron spectroscopy (XPS) was carried out by using a K-alpha X-ray photoelectron spectrometer, Thermal scientific TM.

2.4 Optical, Electrical And Electrochemical Properties

UV-vis spectroscopy was measured by Agilent Cary 60 spectrophotometer. Band gap was calculated according to the Tauc relationship: $\alpha h\nu = B\left(h\nu - \mathrm{E}_g\right)^n$, where α is the absorption coefficient, *hν* is the energy of photon, *B* is a proportionality constant, E_g represents the optical band gap, and *n* is the parameter of specific electronic transition within the band due to the light absorption (n = 1/2, 2 for direct or indirect transition respectively).[12,19,27]

The electrical conductivity (σ) was measured using a four probe set up with a KEITHLEY delta system consisting of an AC and DC current source (model: 6221) and a Nanovoltmeter (model: 2182A) following the formula: $\sigma = \frac{1}{\rho} = \frac{1}{4.532 \times R \times d}$, where, *ρ* is the resistivity of the material. *R* and *d* are the resistance and thickness of the prepared pellet.[12,18,28] The high and low current ranges during the measurement were recorded in the range of 20×10^{-6} to -20×10^{-6} A, and the delta voltage step was fixed at 100 mV s^{-1} for all the samples.

The electrochemical properties were recorded with a PARSTAT 4000 (Princeton Applied Research, USA) electrochemical

View Article Online
DOI: 10.1039/C5RA20928E

workstation using 1 M Na_2SO_4 as the electrolyte. Specific capacitance was calculated from the CV curves using the equation: $C_{CV} = \left(\int I dV\right) / mv$, where C_{CV} is the specific capacitance (F g^{-1}), *I* is the response current density (A g^{-2}), V is the potential window, *υ* is the scan rate (mV s^{-1}), and *m* is the deposited mass on the electrode.[12,29-31] The specific capacitance can be calculated in terms of the discharge time according to the equation: $C_{CD} = I\Delta t / mV$, where C_{CD} is the specific capacitance (F g^{-1}), *I* is the discharging current (A g^{-1}), *V* is the potential window (V) and *m* is the deposited mass on the electrode.[12,30,31] The mass balance of the electrodes for asymmetric configuration, was done according to the relation: $\frac{m_+}{m_-} = \frac{C_- \times \Delta E_-}{C_+ \times \Delta E_+}$, where m_+ and m_- are the mass of the positive and negative electrodes, C_+ and ΔE_+ are the specific capacitance and potential window (calculated from the three electrode measurement) for positive electrode, C_- and ΔE_- are the specific capacitance and potential window of the negative electrode measured at the same scan rate.[12,32,33] The energy density (E_D) and power density (P_D) can be calculated according to the formula, $E_D = CV^2/2$ and $P_D = E_D/\Delta T$, Where C is the specific capacitance, V is the operating voltage, ΔT is the discharge time.[12,33,34]

Results and discussion

The formation of NiO and Fe_3O_4 can be explained by the following reaction mechanism:

$NiSO_4 \rightarrow Ni^{+2} + SO_4^{-2}$

$Ni^{+2} + 2NH_3 + 2H_2O \leftrightarrow Ni(OH)_2 + 2NH_4^+$

$Ni(OH)_2 \rightarrow NiO + H_2O$

$FeSO_4 \rightarrow Fe^{+2} + SO_4^{-2}$

$Fe^{+2} + 3NH_3 + 3H_2O \leftrightarrow Fe(OH)_3 + 3NH_4^+$

$Fe(OH)_3 \rightarrow Fe_3O_4 + H_2O$

Nickel hydroxide and iron hydroxides were formed in presence of $NiSO_4$, $FeSO_4$ and aqueous ammonia solution. However, the hydrothermal process involves high temperature and pressure results in the formation of multi metal oxides of iron and nickel. The hydrothermal reaction was carried out only for 5 h to avoid the formation of spinel phase rather than the single phase metal oxide composite. Extended duration of hydrothermal reaction or high temperature annealing can result in the formation of spinel phase. Figure S1 of the supporting information represents the XRD pattern of F1N2, FN and F2N1. The peaks corresponding to both cubic NiO and Fe_3O_4 are present in all the three composites.[17-20] The relative intensity of the NiO peaks as compared to Fe_3O_4 increased with increasing the concentration of $NiSO_4$ in the precursor. The amount of NiO in comparison to Fe_3O_4 increased from F2N1 to FN and F1N2. The FE-SEM image analysis was carried out for the detailed morphological study of the multi metal composites. The FE-SEM images show that the concentration of nickel oxide plays an important role on the morphology of the composite. Figure 1(a-c) represent the low resolution FE-SEM images of F1N2, FN and F2N1. The composite has cactus like porous structure with higher concentration of NiO (F1N2). The cactus like structure started to distort with increasing the concentration of Fe_3O_4 (FN) and completely destroyed for F2N1. Figure S2(a-c) of the supporting information represent the high magnifying FE-SEM images of F1N2, FN and F2N1. The Fe_3O_4 particles are totally embedded onto the NiO structure for F1N2. The increase in particle size and quite inhomogeneous particle size distribution of NiO and Fe_3O_4 can was noticed in FN. The arbitrarily distributed Fe_3O_4 and NiO particles of F2N1 can be seen from the Figure 1c.

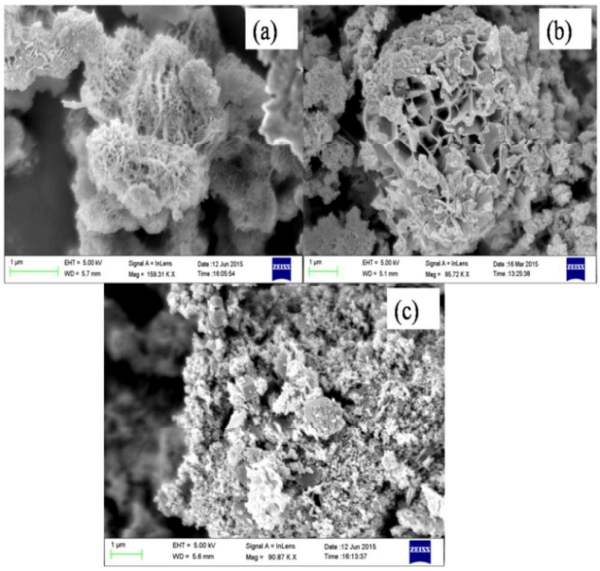

Figure 1. Low resolution FE-SEM image of (a) F1N2, (b) FN and (c) F2N1.

Figure 2a shows the comparison of three electrode CV of F1N2, FN and F2N1. The increase in the current response was noticed with increasing concentration of NiO. The maximum specific capacitance of F2N1, FN and F1N2 are calculated as 500, 583 and 666 F g^{-1}, respectively. The increase in specific capacitance with increasing NiO has been explained by the Nyquist plot analysis. Figure 2b shows the Nyquist plots of F1N2, FN and F2N1. The solution resistance of the composites were comparatively large. The low electrical conductivity of metal oxides may be the reason of such high solution resistance. The slight increase in solution resistance was noticed with the increase of NiO concentration in the composite. The inclination of the Warburg region towards the imaginary axis represented good electrolyte accessibility due to the porous materials or fascinating diffusion path. The FE-SEM images showed that the particle size of NiO/Fe_3O_4 composites decreased with increasing NiO concentration. It is expected that the surface area of the composite increased with decreasing particle size. The Nyquist analysis also showed steeper Warburg region for the composites with higher content of NiO.[18,35] The slope of the Warburg region was very low for the F2N indicating poor porosity as well as low capacitance value. The supercapacitor performance of solo NiO and Fe_3O_4 were tested and compared with the NiO/Fe_3O_4

View Article Online
DOI: 10.1039/C5RA20928E

composite as shown in Fig. S3 of the supporting information. The current responses of the solo metal oxides were poor as compared to the NiO/Fe_3O_4 composite. The specific capacitance was calculated at a scan rate of 10 mV s^{-1} and the results showed prominent increase in specific capacitance for the composite (583 F g^{-1}). The specific capacitances of solo NiO, and Fe_3O_4 were found to be 143 and 294 F g^{-1}, respectively.

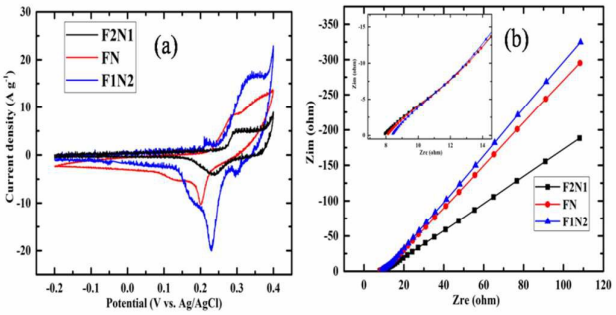

Figure 2. (a) CV and (b) EIS of F1N1, FN and F2N1.

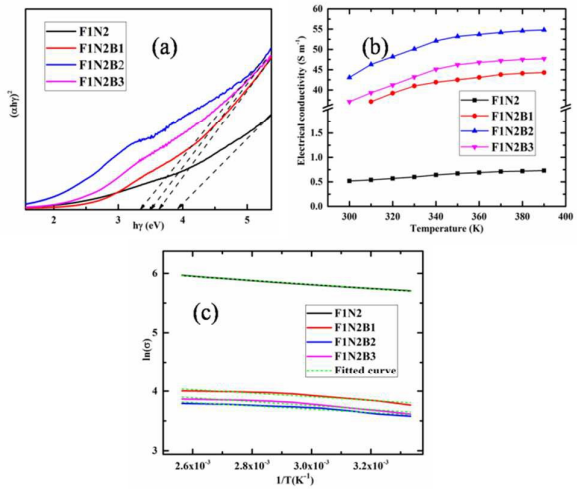

Figure 3.(a) $(\alpha h\nu)^2$ vs $h\nu$ plot, (b) variation of electrical conductivity with temperature and (c) Arrhenius plot of F1N2, F1N2B1, F1N2B2 and F1N2B3.

Figure S4 of the supporting information shows the CV plots of F1N2, FN and F2N1, respectively. The current response of CV increased for all the three composites. The retention of the specific capacitance of the composites has been compared in Figure S5 of the supporting information. The retention is very low for F2N1 and increased with NiO concentration. The good capacitance value may be attributed to the synergistic effect of faradic reaction from NiO and Fe_3O_4. However, the capacitance value was quite low as compared to the theoretical value and the retention is only about ~ 52% at a scan rate of 200 mV s^{-1}. On the basis of the above discussion F1N2 was the best composite for supercapacitor application and the electrical/electrochemical properties of F1N2 was further improved by boron doping.

UV-visible absorption spectroscopy of F1N2 and boron doped composites was carried out to visualize the effect of boron on the electronic property of the multi metal oxide (Figure S6 of supporting information). The significant increase in absorbance intensity noticed with the insertion of boron (for F1N2B1). The absorbance increased for F1N2B2 over F1N2B1 but the intensity decreased with further doping. The $(\alpha h\nu)^2$ vs. $h\nu$ plot of F1N2 and the boron doped composites is shown in Figure 3a. The band gap can be directly calculated from the intersection of the slope to the X-axis.[12,19,27] F1N2 showed a wide band gap of 3.93 eV. Boron doping significantly reduced the band gap of the multi metal oxide. The calculated band gap of F1N2B1 and F1N2B2 were 3.63 and 3.31 eV, respectively. The band gap was increased further in F1N2B3 (3.41 eV) due to B doping into the lattices. The variation of the optical band gap values of multi metal composites can be attributed to the creation of line and/or planar defects due to the boron doping in the crystal structure.[23,25] The doping of boron produced free electrons in the conduction band of the hetero structure multi metal oxide resulting the decrease in band gap energy. The increase in band gap energy ascribed to the excess doping over the optimum level with the higher concentration of boron. The Fermi level energy increased with increasing the doping concentration of electrons resulting the shifting of absorption edge to the higher energies.[36] This phenomenon is called Burstein–Moss effect. [36] The electrical conductivity increased abruptly due to the boron doping. The variation of electrical conductivity of the F1N2 and boron doped composites are shown in Figure 3b. The un-doped F1N2 showed very low electrical conductivity of 0.52 S m^{-1} at room temperature. The electrical conductivity of the multi metal oxide was enhanced by ~50 times with B doping. F1N2B1 and F1N2B2 displayed the electrical conductivity of 25.8 and 43.1 S m^{-1} at room temperature. The decrease in electrical conductivity (37.1 S m^{-1}) noticed for F1N2B3 after further doping. The decrease in electrical conductivity of F1N2B3 may be attributed to the poor carrier mobility at very high concentration of boron.[25] The electrical conductivity increased with temperature for all the composites indicating pure semiconducting nature. Figure 3c shows the linear fitted plot of $ln(\sigma)$ vs. $1/T$. The activation energy was calculated from the slope of the linear fit.[12,37,38] The activation energy of F2N1, F1N2, F1N2B1 and F1N2B2 were 0.29, 0.279, 0.232 and 0.255 eV, respectively. The Nyquist analysis was carried out for the proper understanding of the effect of surface morphology, boron doping and increased electrical conductivity on the electrochemical properties of the multi metal oxides.

The Nyquist result was fitted with ZView software to find out the effect of boron doping on the diffusion path and the diffusion resistance. A perfect semicircle of Nyquist plot is resulted for an electrode involving only EDLC mechanism.[12,18,39] Warburg region is resulted from the pseudo reaction.[12,18,37] Figure 4 shows the Z-View fitted results of F2N1, F1N2, F1N2B1 and F1N2B2. The Warburg impedance (W) represents the route of ion diffusion between the electrode and electrolyte interfaces. W contains three parts: Ohmic resistance (W-R), diffusion time constant (W-T), and

View Article Online
DOI: 10.1039/C5RA20928E

Warburg exponent (W-P).[34,40-42] The origin of the solution resistance is the electrode and electrolyte contact and it depends on the electrical conductivity of the electrode materials.[12,34] Table 1 shows the ZView fitted result of F2N1, F1N2, F1N2B1 and F1N2B2. Both F2N1 and F1N2 were the undoped composite and no significant variation of solution and faradic resistance were noticed. The solution resistance decreased significantly with the insertion of boron. The solution resistance of F2N1, F1N2, F1N2B1 and F1N2B2 were 9.6, 9.4, 5.2 and 1.4 Ω, respectively. The decrease in solution resistance may be attributed to the generation of free electron and increased electrical conductivity of the boron doped composites. The faradic resistance also decreased after boron doping. The diffusion path as well as the diffusion time is an important parameter for the electrode material for enriched supercapacitor performance.[39]

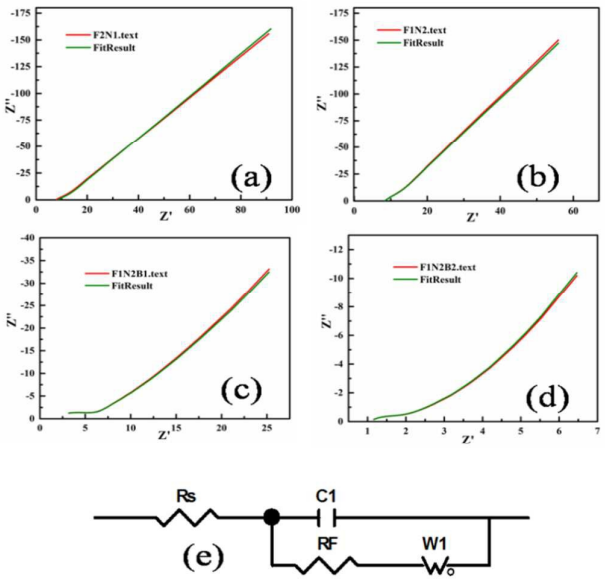

Figure 4. ZView fitted Nyquist plots of (a) F2N1, (b) F1N2, (c) F1N2B1 and (d) F1N2B2. (e) Corresponding equivalent circuit.

Table 1. ZView fitted result of F2N1, F1N2, F1N2B1 and F1N2B2

	Rs	RF	W-R	W-T
F2N1	9.6	3.9	55.9	0.0068
F1N2	9.4	3.9	18.9	0.0048
F1N2B1	5.2	0.3	5.7	0.0037
F1N2B2	1.4	0.29	1.9	0.0022

The diffusion current constant is directly related to the diffusion path.[39] The diffusion current constant of F2N1 and F1N2 are 0.0068 and 0.0048, respectively. The decrease in diffusion path may be attributed to the synergistic effect of high surface area and better incorporation of NiO and Fe_3O_4 particles in F1N2. The diffusion current constant further decreased after boron doping. The low diffusion time constant of F1N2B1 as compared to the F1N2 may be attributed to the creation of huge defect sights and free electrons after boron doping. The formation of free electron elevated the diffusion of charge carrier in the multi metal oxide. The low W-R value of F1N2B1 as compared to the F1N2 also supported the formation of shorter ion diffusion path.[18,35] The low Warburg resistance and diffusion time constant are possibly attributed to the decrease in activation energy of the multi metal oxide. The Arrhenius equation plays a governing role on the chemical kinetics.[38] The diffusion rate is related to the activation energy and the lattice parameter of the materials. The correlation between the activation energy and the electrochemical diffusion has been explained elaborately in the supporting information. The decrease in activation energy of the multi metal composite after boron doping indicated the enhanced ion diffusion through electrode materialds.[38] Furthermore, the Warburg resistance arises from the ionic blocking at the interface of the grain boundary of the electrode materials.[38] The simultaneous decrease in activation energy and W-R suggested enhanced ionic exchange at the interface of the metal oxide grain boundary as the synergistic effect of increasing concentration of NiO and boron doping. The FE-SEM and TEM images of F1N2B2 show that the morphology of the composite remained undistorted after boron doping (Figure S 7a & b of the supporting information). The extensive increase in current response of the multi metal oxide was noticed after the modification of the band gap by boron doping (Figure 5a). The specific capacitance of F1N2, F1N2B1 and F1N2B2 at 10 mV s^{-1} scan rate was measured as 1184, 1467 and 1293 F g^{-1}, respectively. The successive increase and decrease in specific capacitance with different concentration of boron doping shows consistency with the band gap and electrical conductivity analysis.

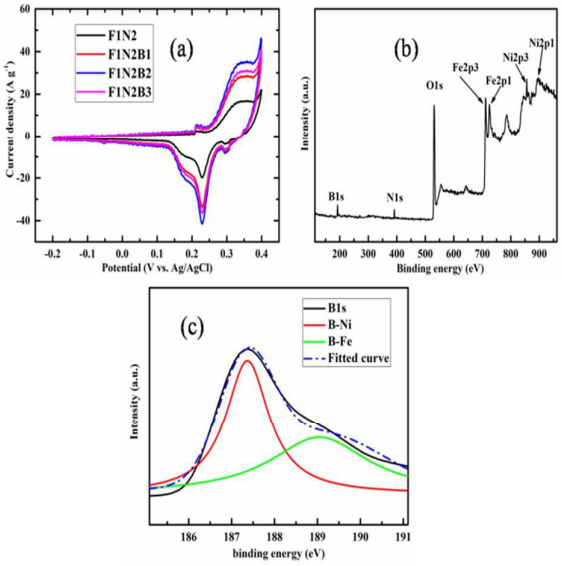

Figure 5. (a) CV plot of F1N2, F1N2B1, F1N2B2 and F1N2B3. (b) XPS survey plot of F1N2B2 and (c) B1s spectrum of F1N2B2.

The CD plot shows the F1N2B2 has IR drop from 0.4 to 0.3 V (Figure S8a of the supporting information). The maximum specific capacitance of 1305 F g^{-1} was achieved at a current

View Article Online
DOI: 10.1039/C5RA20928E

density of 3.5 A g^{-1}. F1N2B2 showed ~ 70% retention in specific capacitance at a high current density of 8 A g^{-1} (Figure S8b of the supporting information). Figure 5b shows the XPS survey spectra of F1N2B2. The peaks at 711, 724.5, 855.6 and 873.1 eV were attributed to the Fe 2p3/2, Fe 2p1/2, Ni 2p3/2 and Ni 2p1/2, respectively.[18,43] The Ni 2p3/2 peak position was different as compared to the metallic Ni (852.7 eV). The energy difference between Ni 2p3/2 and Ni 2p1/2 core levels (~17.5 eV) was also differed from that of the metallic Ni (17.27 eV).[43] The positive shift and the increase in the core level energy difference may be attributed to the +2 valance state of Ni in NiO.[43] The B1s peak appeared at 187.3 eV. The positive shift of the elemental B1s peak as compared to the pure B (187.1 eV) indicates that boron donated its partial electron to the alloying metals.[44] Figure 5c shows the high resolution B1s spectra of F1N2B2. The B1s spectra were deconvoluted in two separate peaks. The peaks at 187.2 and 189.1 eV may be attributed to B-Ni and B-Fe respectively.[45,46] The most intense peak of B-Ni indicates the Bond formation between B and Ni was large as compare to the B-Fe. The B doping ratio was estimated from the XPS peak table analysis. The atomic percentage of boron was calculated as 6.13, 9.71 and 10.6 % for F1N2B1, F1N2B2 and F1N2B3, respectively.

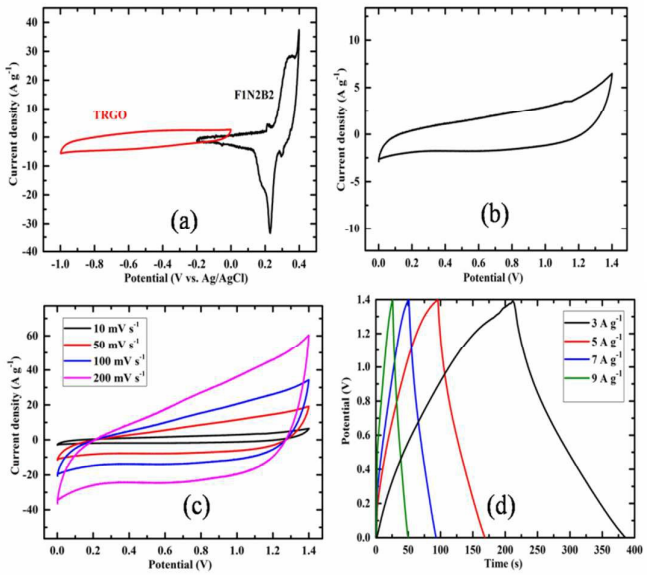

Figure 6. (a) Compare three electrode CV of F1N2B2 and TRGO, (b) CV of ASS, (c) CV of ASS at different scan rate and (d) CD of ASS at different current density.

The specific capacitance of the multi metal oxide composite increased appreciably after boron doping, but still suffered from IR drop of ~0.1 V and small potential window. The asymmetric cell was designed to overcome these limitations. TRGO was used as the negative electrode and the mass deposition ratio of TRGO and F1N2B2 was 1: 52. The CV of TRGO, FIN2B2 and ASS has been compared in Figure 6 (a&b). The CV of ASS at different scan rate is shown in Figure 6c. The CV nature was nearly rectangular and remained undistorted at the higher scan rates. The CD was carried out with different current density from 3 to 9 A g^{-1} and the discharging profile of the CD shows almost zero IR drop. The maximum specific capacitance calculated from the CV was 390 F g^{-1} at a scan rate of 10 mV s^{-1} and the ASS showed good capacitance retention of ~ 60 % at a very high scan rate of 200 mV s^{-1} (Figure S9a of supporting information). The capacitive performance of ASS was studied from the discharging time as shown in Figure S9b of supporting information. The ASS exhibited a specific capacitance of 377 and 157 F g^{-1} at a current density of 3 and 9 A g^{-1}, respectively.

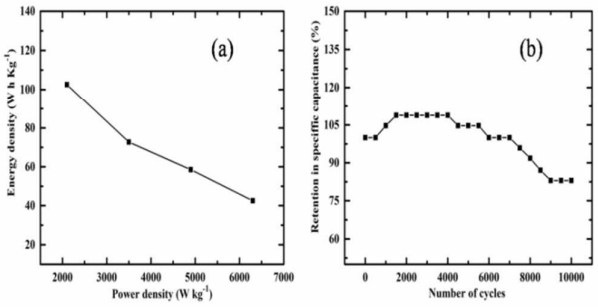

Figure 7. (a) Ragone plot and (b) stability plot of ASS.

Figure 7a shows the Ragone plot of the ASS cell. The large potential window and high specific capacitance value of ASS cell provided a very high energy density of 102.6 W h kg^{-1}. Furthermore, the ASS was able to deliver a huge power density of ~6300 W kg^{-1}. The stability of the ASS cell was tested up to 10,000 cycles. The initial increase in specific capacitance from 500 to 1500 cycles (108 %) may be attributed to the wetting of the electrolyte and enhanced electrode electrolyte contact. The ASS was 100 % stable up to 7000 cycles. The stability decreased to ~82% after 9000 CD cycles and remained constant over 10,000 cycles. The degradation of the electrolyte may be the reason of the deteriorated capacitance.

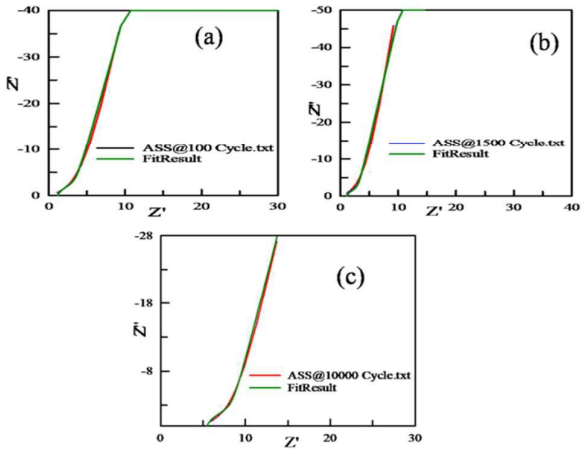

Figure 8. ZView fitted nyquist plot of ASS after (a) 100, (b) 1500 and (c) 10,000 CD cycles.

View Article Online
DOI: 10.1039/C5RA20928E

Table 2. ZView fitted result of ASS@100 cycle, ASS@1500 cycle and ASS@10000 cycle

	Rs	RF	W-R	W-T
ASS@100 Cycle	1.2	0.2	9.9	0.019
ASS@1500 Cycle	1.1	0.2	7.5	0.017
ASS@10000 Cycle	5.5	0.5	9.9	0.039

The Nyquist results of ASS after 100, 1500 and 10,000 CD cycles were fitted with Z-View for the detailed understanding of the variation of capacitance during stability test (Figure 8). The Z-View fitted results were summarized in Table 2. The ASS showed very low solution resistance of ~1.2 ohm and almost zero faradic resistance, during the initial cycles. These parameters remained unchanged after 1500 cycles. The increased specific capacitance of ASS after 1500 cycles was attributed to the improve Warburg impedance. The wetting of the electrode materials decreased the diffusion time constant and Warburg resistance allowing good ion exchange between the electrode materials and electrolyte. The solution and faradic resistance increased after 10,000 cycles possibly due to the degradation of the electrolyte. The increase in the diffusion time constant indicated the relatively poor ion exchange between the electrode materials and electrolyte after 10,000 cycles.

Conclusions

Boron doped NiO/Fe_3O_4 was successfully synthesized by simple one-step hydrothermal method. The increasing concentration of NiO decreased the particle size and the Warburg resistance decreased due to the increased ionic conductivity at the grain boundary of the multi metal oxide. The large band gap of metal oxides was decreased by boron doping. The optimized doping created defects in the multi metal structure to generate large numbers of free electrons. The electrical conductivity increased significantly after boron doping. The synergistic effect of enhanced electrical conductivity and lower activation energy was observed at the lower frequency region of the Nyquist plot. The ZView fitted results showed that the effective diffusion path of the electrode materials decreased after increasing concentration of NiO. The short ion diffusion path and decreased solution resistance enhanced the specific capacitance of the multi metal oxide as a result of boron doping. Very high specific capacitance of 1305 F g^{-1} was achieved at a current density of 3.5 A g^{-1}. However the F1N2B2 suffered for large IR drop and comparatively low rate capability. The ASS cell was developed with TRGO as the negative electrode materials and the CD plot of ASS showed almost zero IR drop. The ASS exhibited good rate capability and a large specific capacitance of 377 Fg^{-1} at a current density of 3 A g^{-1}. The ASS remained ~82% stable even after 10,000 CD cycles tested at a high current density of 9 A g^{-1}. Furthermore, the large energy density of 102.6 W h kg^{-1} and huge power density of ~6300 W kg^{-1} ensured the boron doped NiO/Fe_3O_4 as the potential electrode material for new generation energy storage device.

Acknowledgements

Authors (a&b) are thankful to the Director of CSIR-CMERI. Authors are also thankful to the Department of Science and Technology, New Delhi, India, for the financial support from the DST-INSPIRE Faculty Scheme - INSPIRE Programme (IFA12CH-47) and Council of Scientific and Industrial Research, New Delhi, India, for funding MEGA Institutional project (ESC0112/RP-II). Authors (c&d) would also like to acknowledge the financial support from the R&D Convergence Program of MSIP (Ministry of Science, ICT and Future Planning) of Republic of Korea (Grant CAP-13-2-ETRI).

Notes and references

1 X. Hu, W. Zhang, X. Liu, Y. Mei, Y. Huang, *Chem. Soc. Rev.* **2015**, *44*, 2376-2404.
2 I. Shown, A. Ganguly, L. C. Chen, K. H. Chen, *Energy Sci. Eng.* **2015**, *3*, 2-26.
3 J. D. Lipomi, Z. Bao, *Energy Environ. Sci.* **2011**. *4*, 3314-3328.
4 S. Gao, Y. Sun, F. Lei, L. Liang, J. Liu, W. Bi, B. Pan, Yi. Xie, *Angew. Chem. Int. Ed.* **2014**, *53*, 12789-12793.
5 W. Jiang, D. Yu, Q. Zhang, K. Goh, L. Wei, Y. Yong, R. Jian, J. Wei, Y. Chen, *Adv. Funct. Mater.* **2015**, *25*, 1063-1073.
6 B. Senthilkumar, Z. Khan, S. Park, K. Kim, H. Ko, Y. Kim, *J. Mater. Chem. A*, **2015**, *3*, 21553–21561.
7 L. Li, S. Peng, H. B. Wu, L. Yu, S. Madhavi, X. W. Lou, *Adv. Energy Mater.* **2015**, *5*, 1500753-8.
8 S. Dong, L. Shen, H. Li, P. Nie, Y. Zhu, Q. Sheng, X. Zhang, *J. Mater. Chem. A*, **2015**, *3*, 21277–21283.
9 H. Xia, C. Hong, B. Li, B. Zhao, Z. Lin, M. Zheng, V. S. Savilov, S. M. Aldoshin, *Adv. Funct. Mater.* **2015**, *25*, 627-635.
10 Y. Yang, L. Li, G. Ruan, H. Fei, C. Xiang, X. Fan, J. M. Tour, *ACS Nano* **2014**, *8*, 9622-9628.
11 Wang, R.; Yan, X, *Sci. rep.* **2014**, *4*, 3712.
12 S. Saha, M. Jana, P. Khanra, P. Samanta, H. Koo, N. C Murmu, T. Kuila, *ACS Appl. Mater. Interfaces* **2015**, *7*, 14211-14222.
13 C. Yang, J. Shen, C. Wang, H. Fei, H. Bao, G. Wang, *J. Mater. Chem. A* **2014**, *2*, 1458-1464.
14 R. Zou, F. M. Yuen, Z. Zhang, J. Hu, W. Zhang, *J. Mater. Chem. A* **2015**, *3*, 1717-1723.
15 D. Sarkar, G. G. Khan, A. K. Singh, K. Mandal, *J. Phys. Chem. C* **2013**, *117*, 15523-15531.
16 P. D. Dubal, D. Aradilla, G. Bidan, P. Gentile, S. T. J. Schubert, J. Wimberg, S. Sadki, G. P. Romero, *Sci. Rep.* **2015**, *5*, 09771.
17 B. Zhao, J. Song, P. Liu, W. Xu, T. Fang, Z. Jiao, H. Zhang, Y. Jiang, *J. Mater. Chem.* **2011**, *21*, 18792-18798.
18 S. Saha, M. Jana, P. Samanta, N. C. Murmu, N. H. Kim, T. Kuila, J. H. Lee, *RSC Adv.* **2014**, *4*, 44777-44785.
19 K. Anandan, V. Rajendran, *Nanosci. Nanotechnol. Int. J.* **2012**, *2*, 24-29.
20 H. E. Ghandoor, H. M. Zidan, M. M.H. Khalil, M. I. M. Ismail, *Int. J. Electrochem. Sci.* **2012**, *7*, 5734-5745.
21 X. Hong, J. Kim, S. F. Shi, Y. Zhang, C. Jin, Y. Sun, S. Tongay, J. Wu, Y. Zhang F. Wang, *Nat. nanotechnol.* **2014**, *9*, 167.
22 W. R. Frensley, A volume of VLSI Electronics: microstructure science, San Diego, 1994, pp 1-28.
23 K. W. Noh, Defect engineering of metal oxide semiconductors. University of Illinois at Urbana-Champaign, 2010, Urbana, Illinois.

View Article Online
DOI: 10.1039/C5RA20928E

24 P. Nguyen, H. T. Ng, J. Kong, A. M. Cassell, R. Quinn, J. Li, J. Han, M. McNeil, *Nano Lett.* **2003**, *3*, 925-928.
25 U. Alver, H. Yaykash, S. Kerli, A. Tanrıverdi, *Int. J. Miner., Metall. Mater.* **2013**, *20*, 1097-1101.
26 H. Z Chi, Y. Li, Y. Xin, H. Qin, *Chem. Commun.* **2014**, *50*, 13349-13352.
27 G. Gao, W. Gao, E. Cannuccia, J. T. Tijerina, L. Balicas, A. Mathkar, T. N. Narayanan, Z. Liu, B. K. Gupta, J. Peng, Y. Yin, A. Rubio, P. M. Ajayan, *Nano Lett.* **2012**, *12*, 3518-3525
28 S. Dhibar, P. Bhattacharya, G. Hatui, S. Sahoo, K. C. Das, *ACS Sustainable Chem. Eng.* **2013**, *1*, 1135-1142.
29 J. Yan, Z. Fan, W. Sun, G. Ning, T. Wei, Q. Zhang, R. Zhang, L. Zhi, F. Wei, *Adv. Funct. Mater*. **2012**, *22*, 2632-2641.
30 B. Wang, R. G. Williams, Z. Chang, M. Jiang, J. Liu, X. Lei, X. Sun, *ACS Appl. Mater. Interfaces* **2014**, *6*, 16304-16311.
31 Z. Fan, J. Yan, T. Wei, L. Zhi, G. Ning, T. Li, F. Wei, *Adv. Funct. Mater*. **2011**, *21*, 2366-2375.
32 L. Li, A. Z. Hu, N. An, Y. Y. Yang, M. Z. Li, Y. H. Wu, *J. Phys. Chem. C* **2014**, *118*, 22865-22872.
33 W. Chen, C. Xia, H. N. Alshareef, *ACS Nano* **2014**, *8*, 9531-9541
34 M. Jana, S. Saha, P. Khanra, P. Samanta, H. Koo, N. C. Murmu, T. Kuila, *J. Mater. Chem. A* **2015**, *3*, 7323-7331.
35 Y. Lu, F. Zhang, T. Zhang, K. Leng, L. Zhang, X. Yang, Y. Ma, Y. Huang, M. Zhang, Y. Chen, *Carbon* **2013**, *63*, 508-516.
36 Z. G. Heng, D. X. Yan, X. Hua, X. Gang, *Chin. Phys. B*, **2013**, *22*, 047803.
37 L. K. Sudha, S. Roy, U. K. Rao, *Int. J. Mater., Mech. Manuf*. **2014**, *2*, 96-100.
38 P. Jasinski, V. Petrovsky, T. Suzuki, H. U. Anderson, *J. Electrochem. Soc*. **2005**, *152*, 27-32.
39 B. E. Conway, Electrochemical supercapacitors, New York: Plenum. 1999.
40 N. Zhu, W. Liu, M. Xue, Z. Xie, D. Zhao, M. Zhang, J. Chen, T. J. Cao, *Electrochim. Acta*, **2010**, *55*, 5813-5818.
41 J. Song, M. Z. Bazant, *J. Electrochem. Soc.* **2013**, *160*, 15-24.
42 A. Ehsani, M. G. Mahjani, M. T. Jafarian, *J. Chem.* **2011**, *35*, 735-743.
43 J. Iqbal, B. Wang, X. Liu, D. Yu, B. He, R. Yu, *New J. Phys*. **2009**, *11*, 063009.
44 H. Li, H. Li, W. L. Dai, W. Wang, Z. Fang, J. F. Deng, *Appl. Surf. Sci.* **1999**, *152*, 25-34.
45 J. Legrand, A. Taleb, S. Gota, M. J. Guittet, C. Petit,. *Langmuir* **2002**, *18*, 4131-4137.
46 J. F. Pierson, C. Rousselot, *Surf. Coat. Technol*. **2004**,*180*, 44-48.

View Article Online
DOI: 10.1039/C5RA20928E

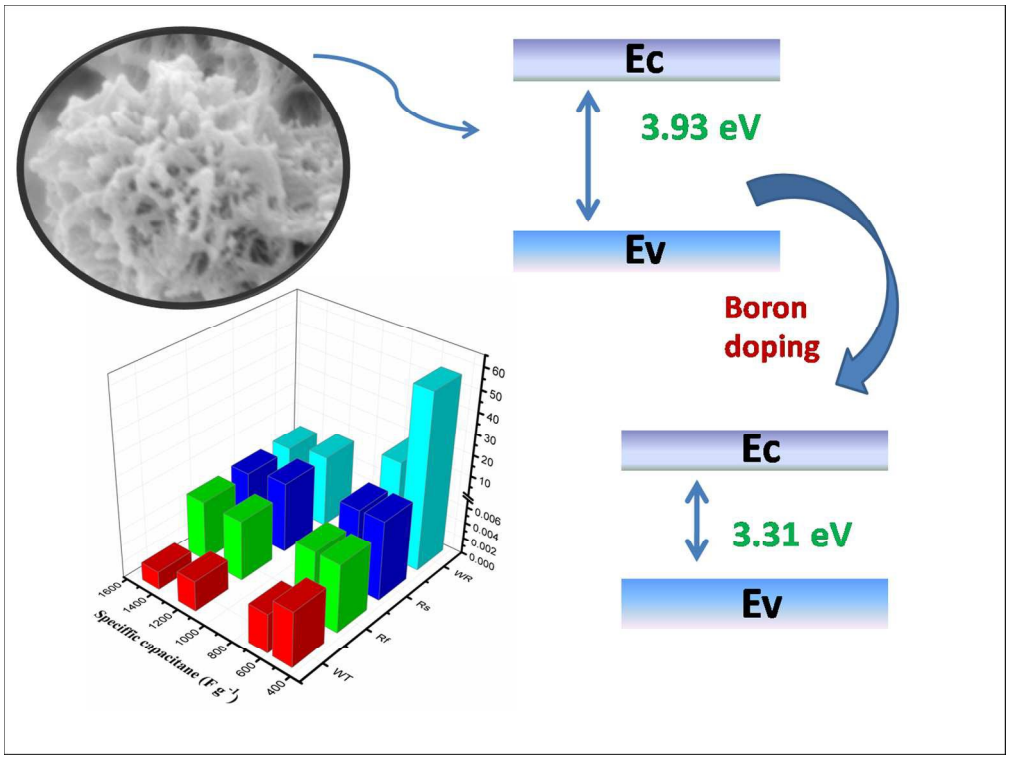

254x190mm (150 x 150 DPI)